



## Mesozoic to Cenozoic magmatic history of the Pamir



James B. Chapman<sup>a,\*</sup>, Shane H. Scoggin<sup>a</sup>, Paul Kapp<sup>a</sup>, Barbara Carrapa<sup>a</sup>,  
Mihai N. Ducea<sup>a,b</sup>, James Worthington<sup>a</sup>, Ilhomjon Oimahmadov<sup>c</sup>, Mustafo Gadoev<sup>c</sup>

<sup>a</sup> Department of Geosciences, University of Arizona, Tucson, AZ 85721, USA

<sup>b</sup> Faculty of Geology and Geophysics, University of Bucharest, 010041, Bucharest, Romania

<sup>c</sup> Institute of Geology, Earthquake Engineering and Seismology, Tajik Academy of Sciences, Dushanbe, Tajikistan

### ARTICLE INFO

#### Article history:

Received 15 July 2017

Received in revised form 1 September 2017

Accepted 18 October 2017

Available online 16 November 2017

Editor: A. Yin

#### Keywords:

Pamir

Tibet

Karakoram

delamination

high-flux

Qiangtang

### ABSTRACT

New geochronologic, geochemical, and isotopic data for Mesozoic to Cenozoic igneous rocks and detrital minerals from the Pamir Mountains help to distinguish major regional magmatic episodes and constrain the tectonic evolution of the Pamir orogenic system. After final accretion of the Central and South Pamir terranes during the Late Triassic to Early Jurassic, the Pamir was largely amagmatic until the emplacement of the intermediate ( $\text{SiO}_2 > 60$  wt.%), calc-alkaline, and isotopically evolved ( $-13$  to  $-5$  zircon  $\varepsilon\text{Hf}_{(t)}$ ) South Pamir batholith between 120–100 Ma, which is the most volumetrically significant magmatic complex in the Pamir and includes a high flux magmatic event at  $\sim 105$  Ma. The South Pamir batholith is interpreted as the northern (inboard) equivalent of the Cretaceous Karakoram batholith and the along-strike equivalent of an Early Cretaceous magmatic belt in the northern Lhasa terrane in Tibet. The northern Lhasa terrane is characterized by a similar high-flux event at  $\sim 110$  Ma. Migration of continental arc magmatism into the South Pamir terrane during the mid-Cretaceous is interpreted to reflect northward directed, low-angle to flat-slab subduction of the Neo-Tethyan oceanic lithosphere. Late Cretaceous magmatism (80–70 Ma) in the Pamir is scarce, but concentrated in the Central and northern South Pamir terranes where it is comparatively more mafic ( $\text{SiO}_2 < 60$  wt.%), alkaline, and isotopically juvenile ( $-2$  to  $+2$  zircon  $\varepsilon\text{Hf}_{(t)}$ ) than the South Pamir batholith. Late Cretaceous magmatism in the Pamir is interpreted here to be the result of extension associated with roll-back of the Neotethyan oceanic slab, which is consistent with similarly aged extension-related magmatism in the Karakoram terrane and Kohistan.

There is an additional pulse of magmatism in the Pamir at 42–36 Ma that is geographically restricted ( $\sim 150$  km diameter ellipsoidal area) and referred to as the Vanj magmatic complex. The Vanj complex comprises metaluminous, high-K calc-alkaline to shoshonitic monzonite, syenite, and granite that is adakitic ( $\text{La}/\text{Yb}_N = 13$  to 57) with low Mg# (35–41). The Vanj complex displays a range of  $\text{SiO}_2$  (54–75 wt.%) and isotopic compositions ( $-7$  to  $-3$   $\varepsilon\text{Nd}_{(t)}$ , 0.706 to 0.710  $^{87}\text{Sr}/^{86}\text{Sr}_{(t)}$ ,  $-3$  to  $+1$  zircon  $\varepsilon\text{Hf}_{(t)}$ , 6.0 to 7.6‰ zircon  $\delta^{18}\text{O}_{\text{VSMOW}}$ ), which reflects some juvenile mantle input and subsequent assimilation or mixing with the Central/South Pamir terrane lower crust. The Vanj complex is speculatively interpreted to be the consequence of a mantle drip or small delamination event that was induced by India–Asia collision. The age, geochemistry, outcrop pattern, and tectonic position of the Vanj magmatic complex suggest that it is part of a series of magmatic complexes that extend for  $>2500$  km across the Pamir and northern Qiangtang terrane in Tibet. All of these complexes are located directly south of the Tanymas–Jinsha suture zone, an important lithospheric and rheological boundary that focused mantle lithosphere deformation after India–Asia collision. Miocene magmatism (20–10 Ma) in the Pamir includes: 1) isotopically evolved migmatite and leucogranite related to crustal anatexis and decompression melting within extensional gneiss domes, and; 2) localized intra-continental magmatism in the Dunkeldik/Taxkorgan complex.

© 2017 Elsevier B.V. All rights reserved.

### 1. Introduction

The Tibetan-Pamir orogen is the preeminent natural laboratory for studying continental collisional orogenesis and is also examined to understand Andean-style orogenesis and oceanic sub-

\* Corresponding author.

E-mail address: jaychapman@email.arizona.edu (J.B. Chapman).

duction that preceded India–Asia collision (Allégre et al., 1984; Yin and Harrison, 2000; Kapp et al., 2007). Magmatic, mostly subduction-related, rocks are a central component of this effort (Ding et al., 2003; Chung et al., 2005; Zhu et al., 2015); however, few syntheses of the magmatic history of the Pamir Mountains, at the western end of the Tibetan plateau exist (Schwab et al., 2004). We present new geochronologic, geochemical, and isotopic data from 14 Mesozoic (pre-collisional) to Cenozoic (syn-collisional) igneous rocks in the Pamir and combine these data with detrital geochronologic and isotopic data to identify and characterize the major magmatic events in the Pamir. Detrital analyses are a powerful tool to obtain an overview of the magmatic history of a region and combining detrital and bedrock analyses allows for more detailed interpretations that are tied to a specific area or magmatic complex. Future studies and additional data from the Pamir will help to improve upon the interpretations presented.

Several discrete magmatic episodes in the Pamir have along-strike equivalents in Tibet or across-strike equivalents in the Karakoram, which are interpreted to reflect orogen-scale geodynamic processes. The magmatic history of the Pamir is used to reconstruct the tectonic evolution of the Tibetan–Pamir orogen from the Cretaceous to the Miocene.

## 2. Geologic background

The Pamir and Tibet are part of a single contiguous orogenic plateau consisting of a series of allochthonous Gondwanan continental fragments that were accreted to Asia during the early Mesozoic (Allégre et al., 1984; Burtman and Molnar, 1993; Robinson et al., 2012). In Tibet, these fragments include the Qiangtang terrane and the Lhasa terrane, separated by the Bangong suture zone (Fig. 1) (Yin and Harrison, 2000). The Qiangtang terrane is laterally equivalent to (from north to south) the Central Pamir terrane, the South Pamir terrane, and the Karakoram terrane, whereas there is no direct equivalent of the Lhasa terrane in the Pamir (Figs. 1 and 2) (Robinson et al., 2012). The Central Pamir terrane was accreted to the Triassic Karakul–Mazar arc-accretionary complex along the Tanyamas suture (Fig. 2) (Burtman and Molnar, 1993) and the Qiangtang terrane was accreted to the Triassic Songpan–Ganzi turbidite complex along the Jinsha suture in Tibet during Late Triassic–Early Jurassic time (Yin and Harrison, 2000). The Karakul–Mazar complex in the Pamir consists of relatively undeformed Late Triassic intermediate intrusive rocks that were emplaced into a Triassic accretionary complex (Schwab et al., 2004; Robinson et al., 2012). The Karakul–Mazar magmatic rocks are believed to have originated above a north-dipping subduction zone (Schwab et al., 2004). Structural relationships exposed in the Muztaghata extensional system (Fig. 2), however, show that the accretionary complex was underthrust southward beneath the Central Pamir terrane and possibly beneath the South Pamir terrane during the Early Jurassic (Robinson et al., 2012). The Central Pamir terrane is separated from the South Pamir terrane by the Rushan–Pshart suture zone (Fig. 2). Southward subduction and closure of the Rushan–Pshart ocean basin during the Jurassic resulted in emplacement of the Rushan–Pshart arc (Schwab et al., 2004). The Karakoram terrane was accreted to the South Pamir terrane along the Tirich–Kilik suture during the Jurassic to Early Cretaceous (Zanchi and Gaetani, 2011).

During the Cretaceous, an Andean-style continental arc associated with the northward subduction of oceanic lithosphere developed on the southern margin of Asia (Searle et al., 1987). The intrusive component of this arc has been called the Trans-Himalayan batholith and consists of the Gangdese batholith in Tibet and the Karakoram batholith in the Pamir (Allégre et al., 1984; Debon et al., 1987). Schwab et al. (2004) suggested that Cretaceous igneous rocks in the South Pamir terrane are part of a composite Tirich–

Mir–Karakoram–Kohistan–Ladakh–Gangdese arc, however, we refer to these rocks as the South Pamir batholith to distinguish them from other magmatic complexes. A belt of Early Cretaceous magmatic rocks in the northern Lhasa terrane in Tibet (distinct from the Gangdese batholith in the southern Lhasa terrane) has been variably interpreted to be related to low-angle northward subduction of Neotethyan oceanic lithosphere (Ding et al., 2003; Kapp et al., 2007), southward subduction of an ocean basin separating the Lhasa and Qiangtang terranes (Zhu et al., 2009), doubly vergent subduction beneath both the Lhasa and Qiangtang terranes (Zhu et al., 2016), and oceanic slab foundering following suturing of the Lhasa and Qiangtang terranes (Chen et al., 2017). This magmatic belt experienced a high flux event at ~110 Ma (Zhu et al., 2009; Sui et al., 2013; Chen et al., 2014).

The timing for the closure of the Neotethyan ocean basin and initial collision of India with Asia is debated. On the Tibetan (east) side of the orogen, estimates for the timing of collision between India and Asia along the Indus–Yarlung suture range from 70 Ma to 25 Ma, with most authors favoring an initial collision at 60–50 Ma (Hu et al., 2016, and references therein). India–Asia collision on the Pamir (west) side of the orogen is complicated by the presence of the Kohistan–Ladakh island arc, which is separated from the Karakoram terrane by the Shyok suture (Fig. 1). Traditionally, Kohistan has been interpreted to have been accreted to the Karakoram terrane in the middle Cretaceous (95–90 Ma) (Searle et al., 1987; Treloar et al., 1989; Borneman et al., 2015), however, other studies have suggested that Kohistan first accreted to India at ~50 Ma and then accreted to the Karakoram terrane at or after ~40 Ma (Bouilhol et al., 2013, and references therein).

Prograde metamorphism in the Karakoram and Pamir suggest that crustal thickening and burial associated with India–Asia collision was underway by the Middle to Late Eocene (Fraser et al., 2001; Smit et al., 2014; Stearns et al., 2013, 2015; Hacker et al., 2017). Structural relationships within the north Karakoram terrane (Zanchi and Gaetani, 2011) and the Central Pamir terrane (Rutte et al., 2017a) also record shortening and crustal thickening during this time. Metamorphism in the Karakoram and Pamir peaked during the Late Oligocene to Early Miocene (Searle et al., 2010; Stearns et al., 2015; Rutte et al., 2017b). Peak metamorphism was immediately followed by the exhumation of a series of extensional gneiss domes (north-south directed extension) in the South and Central Pamir terranes that lasted until the Late Miocene to Early Pliocene (Stübner et al., 2013; Stearns et al., 2013, 2015; Rutte et al., 2017b). These gneiss domes include the Shakhdara–Alichur dome in the South Pamir terrane and the Yazgulem, Sarez, Muskol, and Shatput domes in the Central Pamir terrane (Fig. 2).

### 2.1. Cenozoic magmatism in the Pamir

The most-well studied magmatic rocks in the Pamir are also the youngest; the 10 to 12 Ma potassic Taxkorgan intrusive complex (Robinson et al., 2007; Jiang et al., 2012) and the ultrapotassic Dunkeldik volcanic field (Ducea et al., 2003; Hacker et al., 2005). The Taxkorgan and the Dunkeldik suite magmas have been interpreted to be related to decompression melting and asthenosphere upwelling, which entrained near ultra-high lower crustal xenoliths prior to eruption (Hacker et al., 2005, 2017; Jiang et al., 2012).

The Pamir gneiss domes and the Karakoram metamorphic complex contain abundant early to middle Miocene leucogranite plutons, dikes, and sills as well as leucosomes of similar age in migmatitic regions (Robinson et al., 2007; Searle et al., 2010; Stearns et al., 2015). Previous studies have also identified Eocene igneous rocks in the Central and South Pamir terranes (Schwab et al., 2004; Stearns et al., 2015; Volkov et al., 2016), although there has been no effort to correlate this magmatism along strike

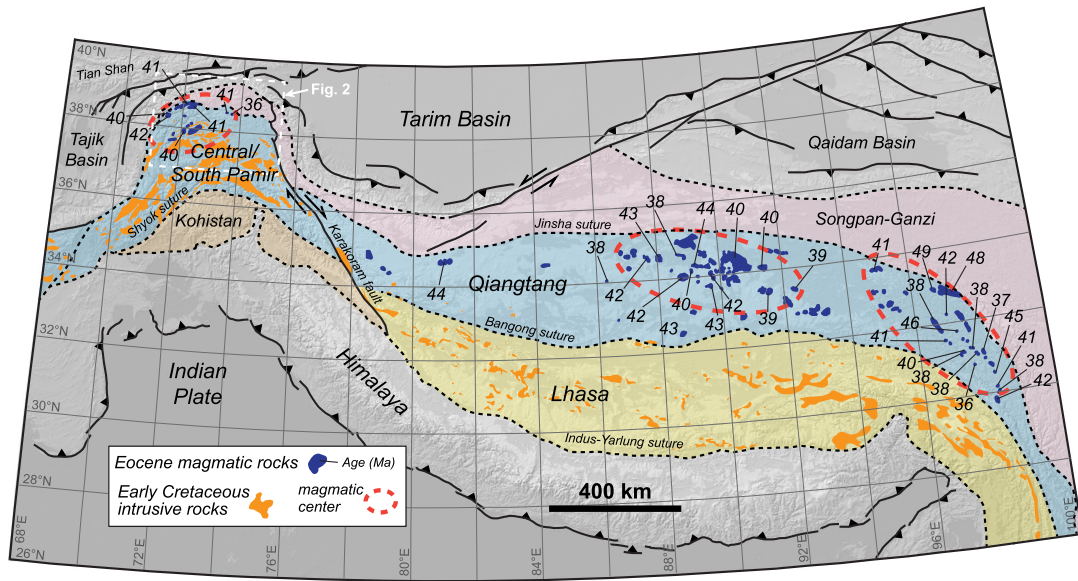


**Fig. 1.** Regional map of the Pamir-Tibetan plateau showing major faults and terrane boundaries. Blue polygons represent Eocene magmatic rocks exposed in the Qiangtang terrane and the laterally equivalent Central/South Pamir terrane. Labels are rock crystallization ages (primarily zircon U–Pb ages). Red dashed lines outline the major Eocene magmatic centers. Eocene magmatic rocks present in other parts of the orogen (e.g., southern Lhasa terrane) are not shown. Orange polygons represent Early Cretaceous intrusive rocks exposed in the central-northern Lhasa terrane and Central/South Pamir and Karakoram terranes. Data sources: (Roger et al., 2000; Ding et al., 2003; Schwab et al., 2004; Jiang et al., 2006; Wang et al., 2008; Zhu et al., 2009, 2016; Chen et al., 2013, 2014; Sui et al., 2013; Long et al., 2015; Stearns et al., 2015; Ou et al., 2017, this study). Map projection: WGS84, UTM z44N. (For interpretation of the references to color in this figure legend, the reader is referred to the web version of this article.)

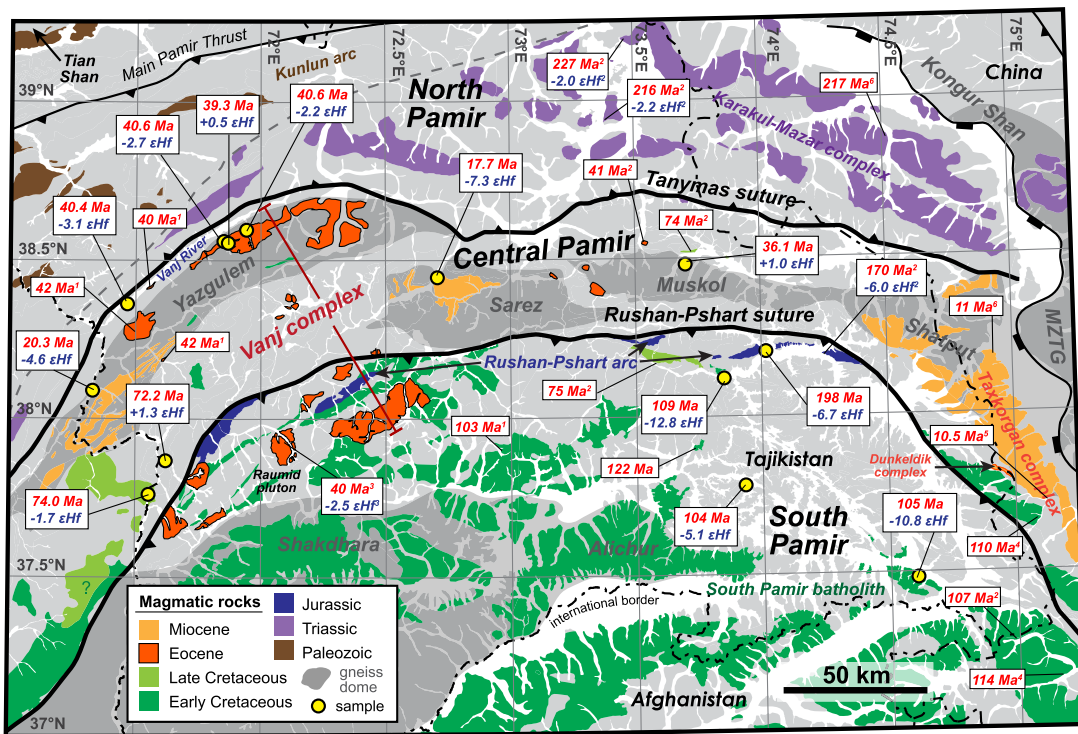


**Fig. 2.** Geologic map of the Pamir Mountains showing exposures of igneous rocks, color-coded by age. For igneous bodies without labels, ages and locations were adopted or modified from Vlasov et al. (1991), Schwab et al. (2004), and Robinson et al. (2012). Non-igneous rocks are shown in light gray and gneiss domes are shown in dark gray. White boxes contain rock crystallization ages in red and zircon  $\epsilon\text{Hf}(t)$  in blue. For comparison purposes, samples with only  $\epsilon\text{Nd}(t)$  values available were converted to  $\epsilon\text{Hf}(t)$  using the terrestrial array of Vervoort et al. (1999). Yellow circles denote samples analyzed in this study. Other sources of data are denoted by superscripts and come from: 1) Stearns et al. (2015); 2) Schwab et al. (2004); 3) Volkov et al. (2016); 4) Jiang et al. (2014); 5) Jiang et al. (2012); 6) Robinson et al. (2007). (For interpretation of the references to color in this figure legend, the reader is referred to the web version of this article.)

or evaluate its tectonic significance. The results presented in this paper suggest that the Eocene igneous rocks are part of single magmatic complex that we refer to as the Vanj complex, because the rocks are most readily accessible along the Vanj river valley in the western Pamir (Fig. 2).

## 2.2. Eocene magmatism in Tibet

Eocene magmatism in Tibet is concentrated in two locations; 1) south of the Jinsha suture in the northern Qiangtang terrane and within the Gangdese batholith along the southern margin of the

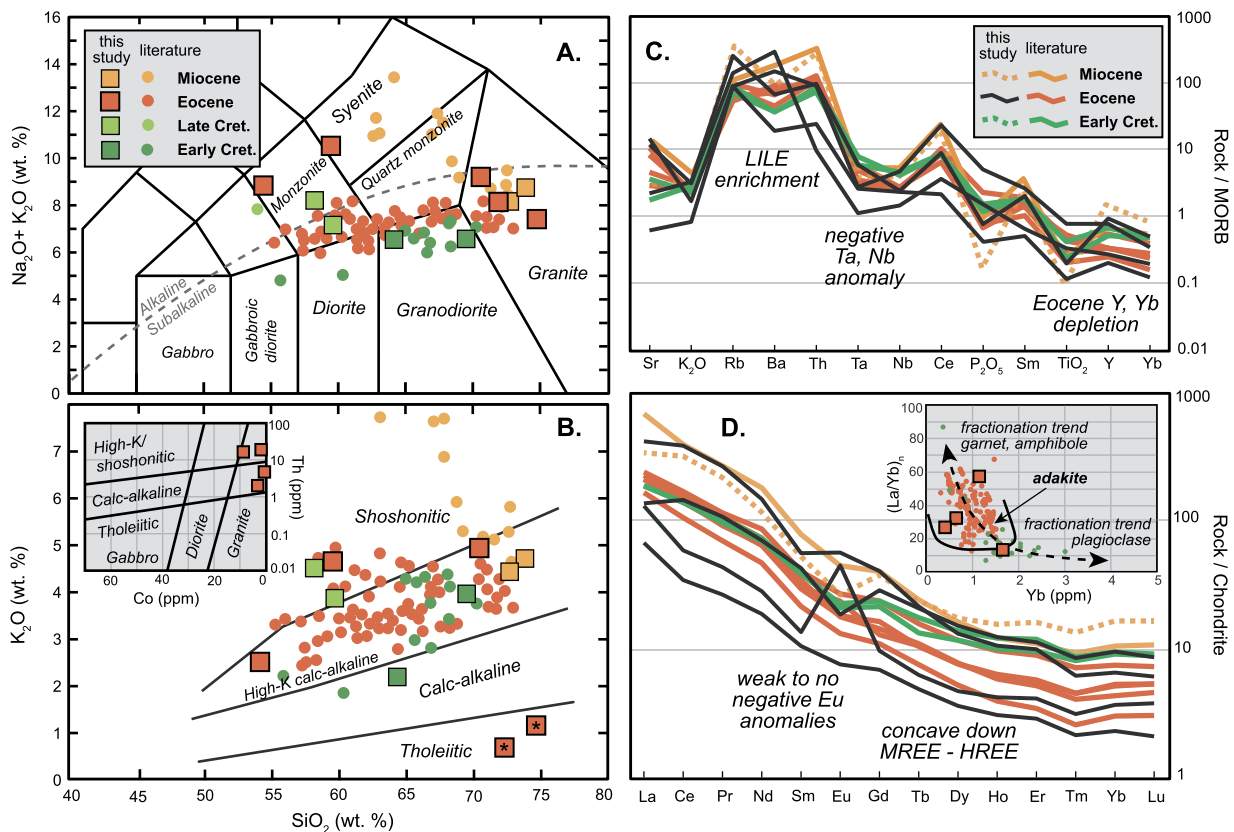


**Fig. 3.** Major and trace element data for samples analyzed in this study and from literature sources. Early Cretaceous literature data are from the South Pamir batholith in the southeastern Pamir (China) (Jiang et al., 2014; J. Li et al., 2016). Eocene literature data are from the northern Qiangtang terrane in Tibet (Wang et al., 2008; Chen et al., 2013; Lai and Qin, 2013; Long et al., 2015; Ou et al., 2017). Miocene literature data come from the Taxkorgan complex (Jiang et al., 2012). A) Total alkali silica diagram. B)  $K_2O$  vs.  $SiO_2$  diagram. Stars mark samples with anomalously low wt.%  $K_2O$  that are interpreted to have lost potassium during hydrothermal alteration (see text). Inset diagram is Co vs. Th, which Hastie et al. (2007) proposed as an alternative to  $K_2O$  vs.  $SiO_2$  diagrams for altered rocks. C) Mid-ocean ridge basalt (MORB) normalized trace element diagram, normalizing values from Pearce and Parkinson (1993), LILE = large-ion lithophile elements. D) Chondrite normalized trace element diagram, normalizing values from McDonough and Sun (1995), MREE = middle rare earth elements, HREE = heavy rare earth elements. Inset shows chondrite normalized  $La/Yb$  vs. Yb, adakitic field from Richards and Kerrich (2007). (For interpretation of the references to color in this figure, the reader is referred to the web version of this article.)

Lhasa terrane (Fig. 1) (Chung et al., 2005). Eocene magmatism in the southern Lhasa terrane, near the India–Asia suture, has been attributed to Neotethyan slab break-off (e.g., Ji et al., 2016, and references therein).

There are several hypotheses concerning the origin of Eocene magmatism at the northern margin of the Qiangtang terrane, including; southward intracontinental subduction of the Songpan-Ganzi terrane (Roger et al., 2000; Ding et al., 2003; Kapp et al., 2005; Wang et al., 2008; Lai and Qin, 2013; Long et al., 2015; Ou et al., 2017), delamination (Chen et al., 2013; Liu et al., 2017), convective removal and upwelling (Guo et al., 2006), and combinations of the above (Jiang et al., 2006).

### 3. Analytical methods

Major elements of eleven rock samples were measured by x-ray fluorescence spectrometry by ALS Global in Vancouver, Canada (Fig. 3; Supplementary Table 1). Whole rock trace elements and Sr and Nd isotopes of five samples were measured by Q-ICP-MS and TIMS, respectively, at the University of Arizona (Figs. 3 and 4; Supplementary Table 1). Zircon U–Pb geochronology (Supplementary Table 2) and zircon Lu–Hf isotope geochemistry (Supplementary Table 3) of fourteen rock samples were analyzed by LA-ICP-MS at the University of Arizona Laserchron Center. Zircon oxygen isotope geochemistry of four rock samples was analyzed by SIMS at the WiscSIMS laboratory at the University of Wisconsin (Supplementary Table 4). Detailed analytical procedures are presented in Supplementary File 1. A summary of sample information, ages, and

isotopic values are presented in Table 1. To help recognize major magmatic events in the Pamir, >1700 Mesozoic and younger detrital zircon U–Pb dates (Fig. 5) and detrital zircon  $\varepsilon Hf(t)$  values (Fig. 6) were compiled from previous studies that sampled major rivers draining the Pamir and Cenozoic sandstone located along the Pamir margins (Supplementary Table 5). Sixty-one new detrital zircons  $\varepsilon Hf(t)$  measurements were made on four sandstone samples from the Tajik Basin that were previously dated by Carrapa et al. (2015) (Fig. 6; Supplementary Table 3).

## 4. Results

### 4.1. Detrital zircon U–Pb and Hf isotopic data

The compilation of previously published detrital zircon U–Pb data (Supplementary Table 5) from the Pamir exhibit a broad Triassic to early Jurassic age peak that matches igneous rock ages from the Triassic Karakul–Mazar arc complex (Schwab et al., 2004; Robinson et al., 2007) (Figs. 2 and 5). There is no distinct Jurassic age peak that records the Jurassic Rushan–Pshart arc (Schwab et al., 2004) (Fig. 5), however, this peak may overlap or be amalgamated with the broad Triassic Karakul–Mazar age peak. Detrital zircon U–Pb dates from 120 Ma to 185 Ma are scarce. The largest age peak in the entire dataset occurs in the middle Cretaceous (~104 Ma) and is consistent with igneous rock ages from the South Pamir batholith (Schwab et al., 2004; Jiang et al., 2014; Stearns et al., 2015; J. Li et al., 2016; this study) (Fig. 2). There are relatively few detrital zircon U–Pb dates between 90 Ma and

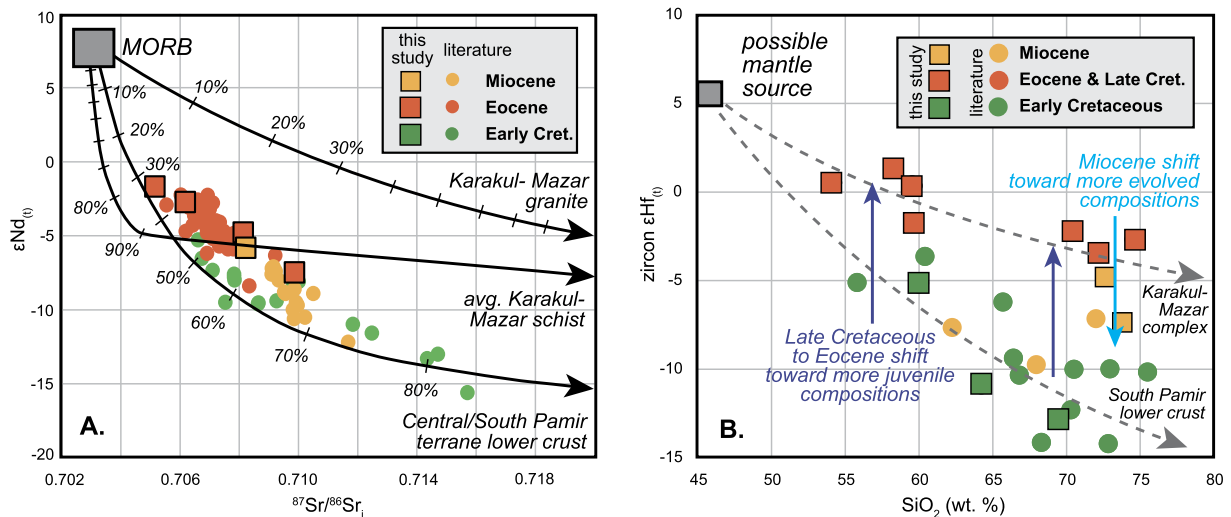


**Fig. 4.** A) Plot of  $\epsilon\text{Nd}(t)$  vs.  $^{87}\text{Sr}/^{86}\text{Sr}_i$  showing three binary mixing lines. All mixing lines use an N-type MORB (mid-ocean ridge basalt) from Sun and McDonald (1989) as the isotopically juvenile end-member. The more isotopically evolved end-members used are: 1) Triassic granite from the Karakul–Mazar complex (Schwab et al., 2004), 2) Triassic schist (metasedimentary accretionary complex material) from the Karakul–Mazar complex (Robinson et al., 2012), and 3) an amphibolite schist from the footwall of the Muztaghata gneiss dome thought to be representative of the Central/South Pamir terrane lower crust (Robinson et al., 2012). Sources of literature data are the same as in Fig. 3. B) Variation in zircon  $\epsilon\text{Hf}(t)$  with  $\text{SiO}_2$  suggests that open-system contamination was important part of magmatic differentiation. Mixing curves and the composition of the juvenile mantle source are for illustrative purposes only and show potential mixing with the Central/South Pamir terrane lower crust and the Karakul–Mazar arc-accretionary complex. Evolved end-member sources are from Schwab et al. (2004) and Robinson et al. (2012). Sources of literature data are the same as in Fig. 3, and only native zircon  $\epsilon\text{Hf}(t)$  (i.e., not converted from  $\epsilon\text{Nd}(t)$ ) is plotted. (For interpretation of the references to color in this figure, the reader is referred to the web version of this article.)

**Table 1**

Summary of geochronologic and isotopic data.

| Sample                           | Lithology    | Age (Ma)       | Latitude (°N) | Longitude (°E) | $\text{SiO}_2$ (wt.%) | $\epsilon\text{Hf}(t)$ | $^{87}\text{Sr}/^{86}\text{Sr}_i$ | $\epsilon\text{Nd}(t)$ | $\delta^{18}\text{O}_{\text{vsmow}}$ (‰) |
|----------------------------------|--------------|----------------|---------------|----------------|-----------------------|------------------------|-----------------------------------|------------------------|--|
| <i>Rushan-Pshart arc</i>         |              |                |               |                |                       |                        |                                   |                        |  |
| 14-73                            | Granodiorite | $198 \pm 7$    | 38.2081       | 74.0284        |                       | $-6.7 \pm 2.6$         | 0.7079 <sup>a</sup>               | $-5.6^a$               |  |
| <i>South Pamir batholith</i>     |              |                |               |                |                       |                        |                                   |                        |  |
| 14-60                            | Granodiorite | $109 \pm 5$    | 38.1289       | 73.8556        | 69.5                  | $-12.8 \pm 2.2$        |                                   |                        |  |
| 14-87                            | Granodiorite | $105 \pm 3$    | 37.4931       | 74.6112        | 64.2                  | $-10.8 \pm 1.7$        |                                   |                        |  |
| 14-89                            | Andesite     | $104 \pm 3$    | 37.7840       | 73.9593        |                       | $-5.1 \pm 2.5$         |                                   |                        |  |
| 13P101                           | Granodiorite | $120 \pm 4$    | 37.9027       | 73.7301        |                       |                        |                                   |                        |  |
| <i>Late Cretaceous magmatism</i> |              |                |               |                |                       |                        |                                   |                        |  |
| 14-37                            | Monzonite    | $74 \pm 2$     | 37.7500       | 71.5667        | 59.6                  | $-1.7 \pm 1.8$         |                                   |                        |  |
| 14-93                            | Monzonite    | $72 \pm 2$     | 37.8735       | 71.6290        | 58.3                  | $1.3 \pm 1.8$          |                                   |                        |  |
| <i>Vanj Complex</i>              |              |                |               |                |                       |                        |                                   |                        |  |
| 14-17                            | Granite      | $40.9 \pm 1.1$ | 38.3618       | 71.4668        |                       | $-3.1 \pm 1.6$         |                                   |                        |  |
| 15-19                            | Syenite      | $36.1 \pm 1.2$ | 38.4839       | 73.6825        | 59.5                  | $1.0 \pm 1.3$          | 0.7062                            | $-2.7$                 | $7.6 \pm 0.3$                            |
| 15-45                            | Granite      | $39.3 \pm 1.5$ | 38.6107       | 71.9441        | 70.4                  | $-2.2 \pm 2.0$         | 0.7099                            | $-7.5$                 | $6.0 \pm 0.3$                            |
| 15-46                            | Monzonite    | $39.8 \pm 1.0$ | 38.5590       | 71.8607        | 54.1                  | $0.5 \pm 2.9$          | 0.7052                            | $-1.7$                 | $6.7 \pm 0.3$                            |
| 15-47                            | Granite      | $40.6 \pm 1.0$ | 38.5602       | 71.8557        | 74.7                  | $-2.7 \pm 1.8$         | 0.7081                            | $-4.8$                 | $7.6 \pm 0.3$                            |
| <i>Gneiss Domes</i>              |              |                |               |                |                       |                        |                                   |                        |  |
| 14-19                            | Granite      | $20.3 \pm 1.3$ | 38.0854       | 71.3219        | 72.7                  | $-4.6 \pm 2.2$         |                                   |                        |  |
| 15-07                            | Granite      | $17.7 \pm 1.0$ | 38.4515       | 72.7031        | 73.8                  | $-7.3 \pm 1.4$         | 0.7082                            | $-5.8$                 |  |

Ages are weighted mean zircon U–Pb ages reported at the  $2\sigma$  level, including both internal and external uncertainties.

$\epsilon\text{Hf}(t)$  values are weighted mean zircon  $\epsilon\text{Hf}(t)$  values reported at the  $2\sigma$  level, including both internal and external uncertainties.

$\delta^{18}\text{O}_{\text{vsmow}}$  values are weighted mean zircon  $\delta^{18}\text{O}_{\text{vsmow}}$  values reported at the  $2\sigma$  level, including both internal and external uncertainties.

Details of analytical procedures and isotopic calculations are presented in Supplementary File 1.

Complete geochronologic, elemental, and isotopic data are presented in Supplementary Tables 1–4.

<sup>a</sup> Data from Schwab et al. (2004).

50 Ma, but there is a small age peak in the Paleocene (~60 Ma). Detrital zircon grains of this age appear in almost all detrital datasets and are most common in Cenozoic sandstones in the Tajik Basin (Carrapa et al., 2015). The origin of this age peak is unclear, it may represent a magmatic suite that has been completely eroded or yet to be identified. The second largest age peak in the dataset occurs in the middle Eocene and matches the ages of igneous rocks in the Vanj complex (Schwab et al., 2004; Stearns et al., 2015; this study) (Figs. 2 and 5). Finally, there are two small age peaks at

~11 Ma and 20 Ma (Fig. 5), which are consistent with igneous rock ages from the Taxkorgan complex (Jiang et al., 2012) and leucogranite from the Pamir gneiss domes (Stübner et al., 2013; Stearns et al., 2015; Rutte et al., 2017b; this study).

Detrital zircon  $\epsilon\text{Hf}(t)$  data help to supplement zircon analyses from igneous rocks and can reveal temporal isotopic trends (Fig. 6). Early Cretaceous zircon Hf isotopic values are clustered between  $-5$  to  $-15$   $\epsilon\text{Hf}(t)$ . The most isotopically juvenile samples ( $>0$   $\epsilon\text{Hf}(t)$ ) in the 100 to 110 Ma range all come from a single

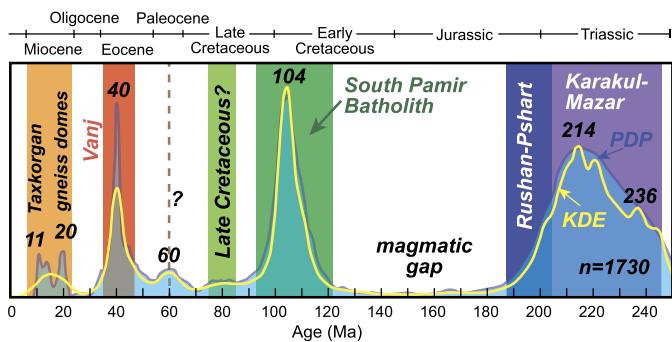


**Fig. 5.** Compiled detrital zircon U-Pb geochronologic analyses from major rivers draining the Pamir and from Cenozoic sandstones on the northern Pamir margin. Data and data sources are reported in Supplementary Table 5. Data without interpretation is shown in Supplementary Fig. 1. Yellow line shows an adaptive kernel density estimate (KDE; bandwidth = 2.34) and the blue line and polygon shows a probability density plot (PDP) for the U-Pb dates (Vermeesch, 2012). The age peaks help to identify major magmatic events and sources within the Pamir Mountains. Vertical bars are the magmatic complexes interpreted to correspond to the age peaks and are color-coded to match the igneous rocks plotted in Fig. 2. (For interpretation of the references to color in this figure legend, the reader is referred to the web version of this article.)

detrital sample (1071-6, Carrapa et al., 2014) (Fig. 6). There is a prominent shift to more isotopically juvenile compositions ( $-5$  to  $+5$   $\varepsilon\text{Hf}_{(t)}$ ) during the Late Cretaceous. Zircon Hf isotopic compositions remain similar ( $-5$  to  $+5$   $\varepsilon\text{Hf}_{(t)}$ ) from the Late Cretaceous to the end of the Eocene, when the detrital zircon Hf record ends.

#### 4.2. The Rushan-Pshart arc and South Pamir batholith

One granodiorite sample (14-73) of the Jurassic Rushan-Pshart arc yielded a zircon U-Pb age  $198 \pm 7$  Ma and an average zircon  $\varepsilon\text{Hf}_{(t)}$  value of  $-6.7 \pm 2.6$  (Table 1). A sample from the same outcrop previously analyzed by Schwab et al. (2004) yielded a whole rock Nd isotopic composition of  $-5.6$   $\varepsilon\text{Nd}_{(t)}$  and a nearby granitic intrusion ( $\sim 170$  Ma), also analyzed by Schwab et al. (2004), yielded a Nd isotopic composition of  $-6.6$   $\varepsilon\text{Nd}_{(t)}$  (Fig. 2). Three granodiorite samples and one porphyritic andesite from the South Pamir batholith were analyzed and have zircon U-Pb ages that range from 120 to 104 Ma and zircon Hf isotopes that range from  $-5$  to  $-13$   $\varepsilon\text{Hf}_{(t)}$  (Table 1). The samples are calc-alkaline to high-K calc-alkaline, metaluminous (aluminum saturation index (ASI)  $[\text{Al}_2\text{O}_3/(\text{CaO} + \text{Na}_2\text{O} + \text{K}_2\text{O}) \text{ mol}\%] = 1.0$  to 1.1), and have Mg# of 38–50 (Fig. 3), consistent with other analyses of igneous rocks from the South Pamir batholith (Schwab et al., 2004; Jiang et al., 2014; J. Li et al., 2016).

#### 4.3. Late Cretaceous magmatism

Two monzonite samples, 14-37 and 14-93, were collected and yielded zircon U-Pb ages of  $72 \pm 2$  Ma and  $74 \pm 2$  Ma, respectively (Table 1; Fig. 2). Ages are concordant and there is no evidence for zircon inheritance. The similarity of the ages of these samples to a pair of Late Cretaceous magmatic rocks reported in Schwab et al. (2004) (Fig. 2) suggest that this may be a distinct magmatic event. However, there is no obvious corresponding age peak in the detrital zircon U-Pb record (Fig. 5), which may indicate a local and/or low-volume magmatic event. The two samples analyzed contain modal biotite and amphibole, are weakly shoshonitic (4–5 wt.%  $\text{K}_2\text{O}$ ), metaluminous (ASI = 0.9 to 1.0), and have Mg# of 36 to 44. Average zircon Hf isotopic compositions for the 74 Ma and 72 Ma samples are relatively high,  $-1.7$  to  $+1.3$   $\varepsilon\text{Hf}_{(t)}$  and are more isotopically juvenile than any sample from the South Pamir batholith (Fig. 2).

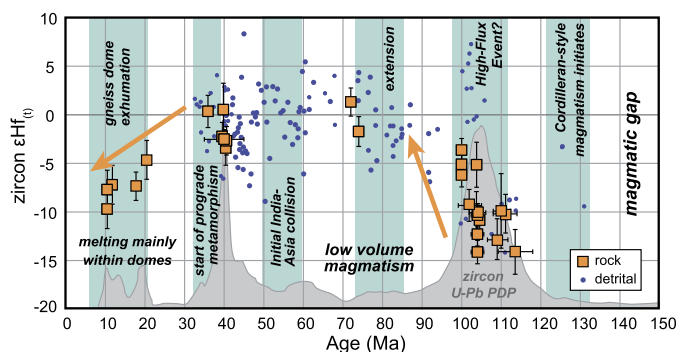


**Fig. 6.** New and compiled zircon  $\varepsilon\text{Hf}_{(t)}$  data plotted against zircon U-Pb ages. Weighted mean zircon  $\varepsilon\text{Hf}_{(t)}$  from rock samples are plotted as squares with  $2\sigma$  uncertainty error bars, single detrital zircon  $\varepsilon\text{Hf}_{(t)}$  analyses are plotted as blue dots. Only native  $\varepsilon\text{Hf}_{(t)}$  data is plotted. Isotopic data for rock samples come from this study (Table 1) and from literature sources listed in Fig. 3. Isotopic data for detrital zircon come from this study (Supplementary Table 3) and from Carrapa et al. (2014) and Sun et al. (2016). The zircon U-Pb probability density plot (PDP) shown in gray is reproduced from Fig. 5. Vertical blue bars denote interpreted tectonic events for the Pamir. Data without interpretation is shown in Supplementary Fig. 1. (For interpretation of the references to color in this figure legend, the reader is referred to the web version of this article.)

#### 4.4. The mid-Eocene Vanj magmatic complex

Five samples were collected from the Vanj magmatic complex (14-17, 15-19, 15-45, 15-46, and 15-47). Interpreted zircon U-Pb ages from these samples range from 41 to 36 Ma (Table 1). Most single spot U-Pb zircon rim and core analyses overlap within uncertainty (Supplementary Table 2). Those that did not were not included in the weighted mean age interpretations. The Vanj complex rocks have not been documented north of the Tanyamas suture (Fig. 2). The rocks are exposed in both the footwalls and hanging walls of the Central Pamir gneiss domes (Yazgulem, Sarez, and Muskul domes) and are concentrated in an  $\sim 150$  km diameter circular region south of the Vanj river (Fig. 2).

The Vanj complex samples are monzonite, syenite, and granite. The samples are generally high-K calc-alkaline to shoshonitic, except for samples 14-17 and 15-47, which have anomalously low wt.%  $\text{K}_2\text{O}$  and plot within the tholeiitic field in a  $\text{K}_2\text{O}$  vs. silica diagram (Fig. 3A). However, these specific samples also have low wt.%  $\text{Fe}_2\text{O}_3$  and MgO and plot within the evolved calc-alkaline region on alkaline-total Fe-MgO (AFM) ternary diagram. Samples 14-17 and 15-47 were collected from within the Yazgulem gneiss dome and show evidence for some hydrothermal alteration, including sericitic alteration of feldspar in thin-section. Potassium depletion is a known problem in altered rocks and Hastie et al. (2007) have suggested using Th vs. Co (fluid immobile elements) diagrams in place of  $\text{K}_2\text{O}$  vs. silica plots. Samples 14-17 and 15-47 plot in the calc-alkaline to high-K calc-alkaline fields on these diagrams (Fig. 3B) and are interpreted to be altered high-K calc-alkaline rocks. The Vanj magmatic complex samples have low Mg# (35–41) and are metaluminous (ASI = 0.95 to 1.04). On a mid-ocean ridge basalt (MORB) normalized trace element diagram (Fig. 3C), the Vanj magmatic complex samples are enriched in LILE and depleted in high field strength elements (HFSE) with negative Ta and Nb anomalies. The samples have concave up chondrite normalized REE patterns, are moderately depleted in HREE (e.g., Y and Yb), and plot within the adakitic field on La/Yb vs. Yb diagrams (Fig. 3D). The samples have weak to no negative Eu anomalies and sample 15-19 has a strong positive Eu anomaly.

For the Vanj complex samples, whole rock initial Sr isotopes range from 0.705 to 0.710  $^{87}\text{Sr}/^{86}\text{Sr}_i$ , whole rock initial Nd isotopes range from  $-1.7$  to  $-7.5$   $\varepsilon\text{Nd}_{(t)}$ , and average zircon initial Hf isotopes range from  $-3.1$  to  $+1.0$   $\varepsilon\text{Hf}_{(t)}$  (Table 1). The sample (14-17) with the most negative zircon  $\varepsilon\text{Hf}$  value ( $-3.1$   $\varepsilon\text{Hf}_{(t)}$ ) is

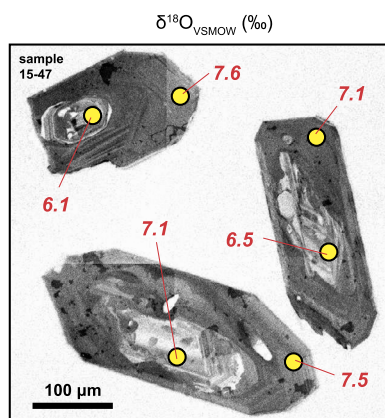


**Fig. 7.** Representative cathodoluminescence (CL) images of polished zircon crystals from sample 15-47 from the Eocene Vanj magmatic complex in the Pamir. Individual zircon  $\delta^{18}\text{O}$  secondary ion mass spectrometer (SIMS) analysis locations are shown by yellow circles and zircon  $\delta^{18}\text{O}$  values (red text) are reported in ‰ relative to Vienna standard mean ocean water (VSMOW). Sample 15-47 is the only sample that showed systematic differences in zircon  $\delta^{18}\text{O}$  between zircon rims and cores. (For interpretation of the references to color in this figure legend, the reader is referred to the web version of this article.)

the only sample that contains dates interpreted as inherited ages in zircon cores. Average zircon  $\varepsilon\text{Hf}(t)$  and whole rock  $\varepsilon\text{Nd}(t)$  decrease with increasing wt.%  $\text{SiO}_2$  (Fig. 4). Zircon oxygen isotopes ( $\delta^{18}\text{O}_{\text{VSMOW}}$ ) in the samples range from 6.0 to 7.6‰ (Table 1). There is no clear relationship between zircon  $\delta^{18}\text{O}$  and  $\text{SiO}_2$ . Zircon cores and rims from most samples have similar average  $\delta^{18}\text{O}$  values, although sample 15-47 has an average  $\delta^{18}\text{O}$  of 6.5‰ in zircon cores and 7.6‰ in zircon rims, despite no U–Pb age difference between zircon rims and cores in this sample (Fig. 7).

#### 4.5. Miocene gneiss dome magmatism

Two leucogranite samples were analyzed, one from the Yazgulem (14-19) and one from Sarez (15-07) gneiss domes (Fig. 2). Both samples are high-K calc-alkaline granite with zircon U–Pb crystallization ages of ~18–20 Ma (Table 1). Zircons from the gneiss dome samples have abundant inherited cores (Supplementary Table 2). The samples have average zircon Hf isotopes of –4.6 to –7.3  $\varepsilon\text{Hf}(t)$  (Table 1, Fig. 2). Sample 15-07 has a whole rock Sr isotopic value of 0.708  $^{87}\text{Sr}/^{86}\text{Sr}_i$  and an Nd isotopic value –5.8  $\varepsilon\text{Nd}(t)$  (Table 1). These samples are among the most felsic magmatic rocks in the Pamir (>70 wt.%  $\text{SiO}_2$ , Mg# 18–24) and are metaluminous (ASI = 1.0). Sample 15-07 displays LILE enrichment and negative Ta and Nb anomalies in a MORB-normalized trace element plot and has minor HREE depletion enrichment ( $\text{Sr}/\text{Y} = 8$ ,  $(\text{La}/\text{Yb})_N = 19$ ) (Fig. 3).

## 5. Discussion

### 5.1. Isotopic composition of Pamir lithosphere

In the footwall of the Muztaghata extensional system, Robinson et al. (2012) identified upper amphibolite facies schist that may be representative of Central/South Pamir terrane lower crust. The most isotopically evolved sample from that study (sample 9-4-03-1) is a plausible end-member in  $\varepsilon\text{Nd}$ – $^{87}\text{Sr}/^{86}\text{Sr}$  binary isotopic mixing models for the rocks of the South Pamir batholith (Fig. 4A). A plot of  $\varepsilon\text{Hf}(t)$  vs.  $\text{SiO}_2$  suggests that the South Pamir batholith and the Late Cretaceous to Eocene magmatic rocks in the Central Pamir terrane assimilated more isotopically evolved crustal material during differentiation (Fig. 4B). The Central/South Pamir terrane lower crust samples from Robinson et al. (2012) have

isotopic values of –9 to –15  $\varepsilon\text{Nd}(100)$  (the  $\varepsilon\text{Nd}$  isotopic composition at 100 Ma), consistent with the Early Cretaceous assimilation trend in Fig. 4B. In contrast to the South Pamir batholith samples, the Late Cretaceous and Eocene magmatic rocks in the Central Pamir terrane require more isotopically juvenile end-members with higher Sr/Nd for viable binary mixing models (Fig. 4A).

During the Late Triassic, the Karakul–Mazar arc-accretionary complex was Underthrust ~100 km beneath the Central Pamir terrane (Robinson et al., 2012). It is possible that the majority of the deep lithosphere in the Central Pamir terrane consists of Karakul–Mazar complex material, which is a potential isotopically evolved end-member for the assimilation trend for the Late Cretaceous and Eocene magmatic rocks in Fig. 4B. The metasedimentary and igneous rocks of the Karakul–Mazar complex have  $\varepsilon\text{Nd}(40)$  values of –5 to –9 (Schwab et al., 2004; Robinson et al., 2012). However, the Sr and Nd isotopic composition of the Eocene magmatic rocks is better fit by a mixing model with a relatively evolved (<–10  $\varepsilon\text{Nd}(t)$ ) end-member similar to the Central/South Pamir terrane lower crust and input from a depleted mantle source (Fig. 4A).

## 6. Magmatic history of the Pamir

The new and compiled geochemical and geochronologic data for the Pamir help to constrain and clarify the Mesozoic to recent tectonic history of the Pamir Mountains and allow comparisons to magmatism in other parts of the broader orogenic system (Karakoram–Kohistan–Himalaya–Tibet). A series of schematic cross-sections is presented in Fig. 8, which depicts the Pamir orogen during each of the major magmatic events since the Cretaceous.

### 6.1. Early to mid-Cretaceous

Geochemical data suggests that the calc-alkaline South Pamir batholith represents part of an Early Cretaceous continental arc, which we interpret to be equivalent to the Cretaceous Karakoram batholith (Searle et al., 1987; Schwab et al., 2004) and an Early Cretaceous magmatic belt in the northern Lhasa terrane (Zhu et al., 2009). The oldest and youngest samples that have been dated from the South Pamir batholith are 120 Ma and 104 Ma (Fig. 2; Table 1) and the detrital zircon U–Pb data suggest that most magmatism occurred between 120 and 90 Ma with a higher volumetric output at ~105 Ma (Fig. 5). Subduction-related magmatism in the Karakoram batholith occurred from ~130 Ma to 95 Ma, and there is a cluster of ages between 110 and 105 Ma that may represent a high-flux event (Debon et al., 1987; Fraser et al., 2001; Heuberger et al., 2007). Magmatism was also active in Kohistan during the Early Cretaceous, supporting models for two north-dipping subduction zones (Fig. 8) (Burg, 2011). Early Cretaceous magmatism in the northern Lhasa terrane occurred from 130 Ma to 105 Ma, with a high-flux event at ~110 Ma (Zhu et al., 2009; Sui et al., 2013; Chen et al., 2014).

The South Pamir batholith is presently located up to 200 km north of the Shyok suture and the Early Cretaceous magmatic belt in the northern Lhasa terrane is located up to ~300 km north of the Indus-Yarlung suture (Fig. 1). These distances do not include a restoration of post-magmatic shortening. Because the Central Pamir and South Pamir terranes were sutured together prior to emplacement of the South Pamir batholith (Schwab et al., 2004), southward directed subduction cannot explain the batholith. A period of low-angle to flat subduction may be required during the Early Cretaceous to generate magmatism in the South Pamir terrane so far from the subduction margin (Fig. 8). The Pamir was also actively shortening during this time (Robinson, 2015) and low-angle to flat subduction may have influenced this early phase of orogenesis.

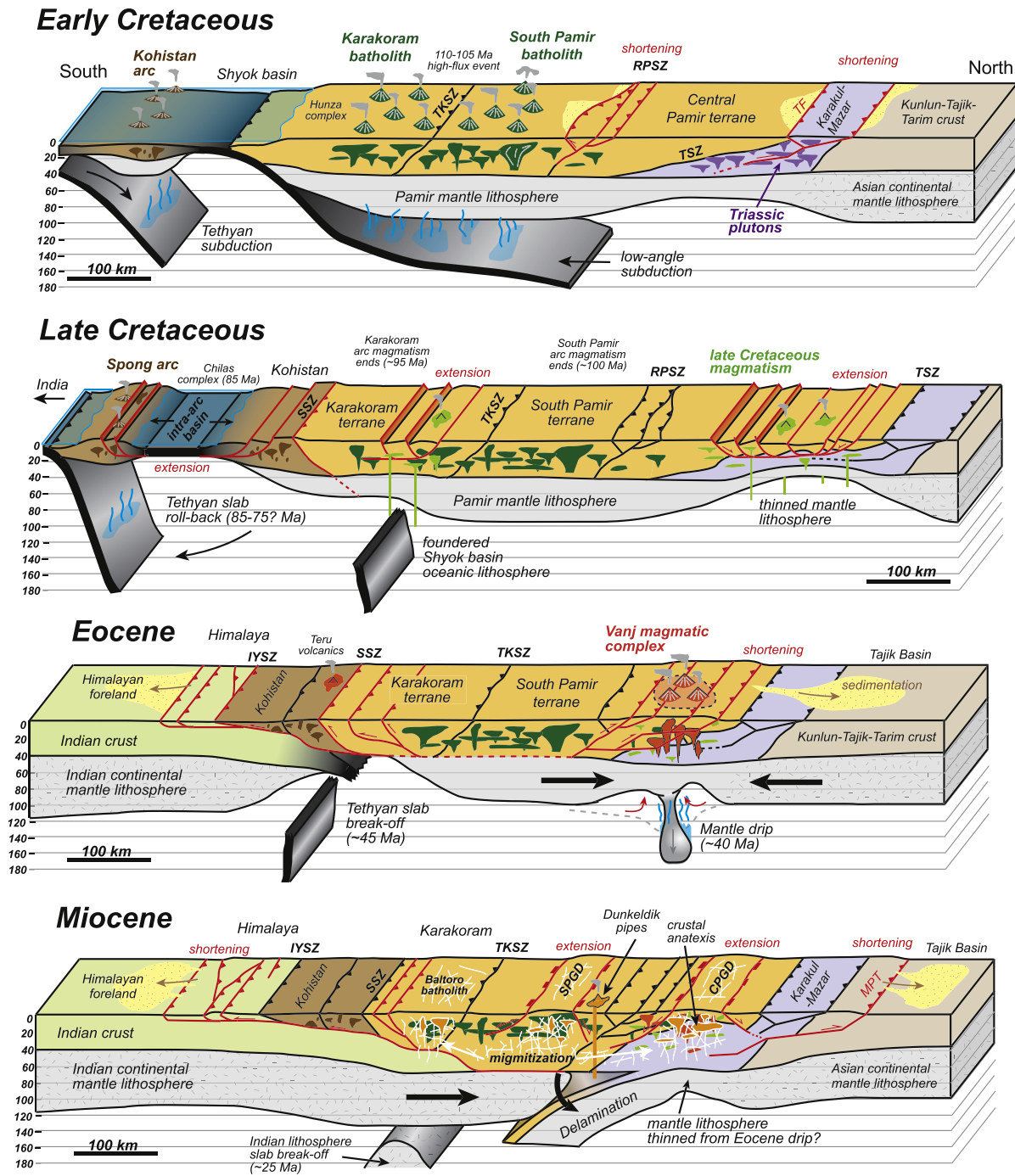


**Fig. 8.** Schematic cross-sections for the Pamir orogenic system at different periods in the past that show some of the major tectonic and magmatic events that have affected the Pamir. Details of the cross-sections are discussed at length in section 6 of this report. Early Cretaceous) Low-angle subduction of Shyok basin oceanic lithosphere resulted in emplacement of the South Pamir and Karakoram batholiths. Late Cretaceous) Foundering of Shyok basin oceanic lithosphere and roll-back of the Neotethyan oceanic slab resulted in extension and extension-related magmatism in Kohistan, the Karakoram, and the Pamir. Eocene) Localized thickening of the mantle lithosphere during India-Asia collision occurred near a rheological boundary between the structurally and magmatically weakened Central/South Pamir terrane and strong North Pamir-Tarim basement. Negative buoyancy of the thickened mantle lithosphere led to the development of a mantle drip or small delamination event. Eocene igneous rocks in the Karakoram terrane are attributed to break-off of the Neotethyan slab. Miocene) Formation of leucogranite and migmatite within the Karakoram metamorphic complex and Pamir gneiss domes are attributed to crustal anatexis and syn-extensional decompression melting. TKSZ = Tirich-Kilik suture zone, RPSZ = Rushan-Pshart suture zone, TSZ = Tanymas suture zone, TF = Tanymas fault, SSZ = Shyok suture zone, IYSZ = Indus-Yarlung suture zone, SPGD = South Pamir gneiss domes, CPGD = Central Pamir gneiss domes, MPT = Main Pamir thrust. (For interpretation of the references to color in this figure, the reader is referred to the web version of this article.)

## 6.2. Late Cretaceous

The end of subduction-related magmatism in the Karakoram and South Pamir batholiths is interpreted to reflect suturing of the Kohistan island arc with the Karakoram terrane at ~90 Ma, along the Shyok suture zone (Pettersen and Treloar, 2004; Borneman et

al., 2015). Evidenced in part by the ~85 Ma Chilas magmatic complex (Jagoutz et al., 2007), Kohistan is thought to have experienced intra-arc extension and the development of an intra-arc basin during the Late Cretaceous, which has been linked to Neo-Tethyan slab roll-back (Treloar et al., 1989; Burg, 2011). This extension may have split Kohistan into two arcs and there is evidence in the

Ladakh region for the presence of a second island arc system, the Spong arc, located south of the main Kohistan arc (Corfield et al., 2001) (Fig. 8). Late Cretaceous extension is recorded in the Karakoram terrane by mafic alkaline magmatism (~88 Ma; Debon and Ali-Khan, 1996). This magmatism may also be related to break-off and foundering of Shyok basin oceanic lithosphere following collision of the Kohistan arc (Fig. 8).

Late Cretaceous magmatic rocks (~75 Ma) in the Pamir are relatively alkaline and mafic (Fig. 3) and the most mafic samples from the Late Cretaceous and Eocene magmatic complexes are ~5  $\epsilon\text{Hf}_{(t)}$  units higher than the most mafic samples from the Early Cretaceous South Pamir batholith (Figs. 4 and 6). The shift from isotopically evolved to more isotopically juvenile magmatism during the Late Cretaceous is consistent with enhanced juvenile (depleted mantle) magmatic input and is interpreted to reflect a period of lithospheric extension (Fig. 8). Back-arc rifting in other convergent orogens has been associated with shifts to more isotopically juvenile magmatism (Kemp et al., 2009). Thinned or modified mantle lithosphere, associated with underthrusting of the Karakul–Mazar accretionary complex beneath the Central Pamir terrane during the early Mesozoic, may have helped localize Late Cretaceous extensional deformation in the Central Pamir terrane, as there is no evidence that the South Pamir terrane experienced extension during this time. In addition to the Late Cretaceous magmatic rocks described in this study, Rutte et al. (2017a) reported a basalt flow within a Maastrichtian(?) section in the Central Pamir terrane that may be related to the proposed extensional event.

### 6.3. Eocene

A Neotethyan oceanic slab-break off event has been proposed for the Tibet–Karakoram–Pamir region at ca. 45 Ma (Chemenda et al., 2000; Replumaz et al., 2010; Smit et al., 2014), which may have produced the ~44 Ma Teru/Shamran volcanic group along the Shyok suture (Khan et al., 2004; Petterson and Treloar, 2004). The spatially restricted Vanj magmatic complex in the Pamir is located 300–400 km north of the Indus suture and is considered unlikely to be related to foundering of the Neotethyan slab.

We interpret the Vanj magmatic complex to be an along-strike equivalent of the Eocene magmatic complexes in the northern Qiangtang terrane (Ding et al., 2003; Wang et al., 2008; Long et al., 2015). The Vanj and northern Qiangtang complexes are both located directly south of the Jinsha–Tanyamas suture zone and are clustered into a series of ellipsoidal “centers” that are up to a few hundred kilometers in diameter (Fig. 1). The Vanj and north Qiangtang complexes were erupted or emplaced within a narrow time range during the Eocene: 42–36 Ma for the Vanj complex (Schwab et al., 2004; Stearns et al., 2015; this study), 44–38 Ma for the north-central Qiangtang terrane (Ding et al., 2003; Wang et al., 2008; Chen et al., 2013; Lai and Qin, 2013; Long et al., 2015; Ou et al., 2017) and 49–36 Ma for the eastern Qiangtang terrane (Roger et al., 2000; Jiang et al., 2006; Liu et al., 2017) (Fig. 1). Detrital zircon U–Pb data suggest a peak in magmatism at ~40 Ma in the Pamir (Fig. 5) and Chen et al. (2013) reported a magmatic peak (marked by a predominance of zircon dates) at ~42 Ma in the north Qiangtang terrane. The geochemistry of the northern Qiangtang terrane magmatic rocks and the Vanj magmatic complex rocks in the Pamir are similar. Both complexes are intermediate in composition, high-K calc-alkaline to moderately shoshonitic, metaluminous to weakly peraluminous, have pronounced negative Nb and Ta anomalies in MORB normalized trace element variation diagrams, are LREE-enriched, HREE-depleted, have relatively low Y and Yb contents, classified as adakitic, have small to no negative Eu anomalies, have Nd isotopic compositions of  $-3$  to  $-7$   $\epsilon\text{Nd}_{(t)}$ , and  $^{87}\text{Sr}/^{86}\text{Sr}_i$  ratios of 0.706

to 0.710 (Wang et al., 2008; Chen et al., 2013; Lai and Qin, 2013; Long et al., 2015; Ou et al., 2017; this study).

One explanation for the Eocene magmatic event in the northern Qiangtang terrane is that continental lithosphere of the Songpan–Ganzi terrane was subducted southward beneath the Qiangtang terrane (intracontinental subduction model) in response to India–Asia collision (Roger et al., 2000; Ding et al., 2003; Kapp et al., 2005; Spurlin et al., 2005; Wang et al., 2008; Lai and Qin, 2013; Long et al., 2015; Ou et al., 2017). This model is appealing because Eocene magmatism did not occur north of the Tanyamas–Jinsha suture (Fig. 1). However, it is unclear if intracontinental subduction produces magmatism as there is no modern volcanism associated with intercontinental subduction of Indian continental lithosphere beneath Tibet (Chung et al., 2005; Zhu et al., 2015). Also, while there is evidence for Eocene shortening in northern Tibet, most of this shortening occurred south of the Jinsha suture and the absolute magnitude of shortening is modest (<100 km) (Kapp et al., 2005; Spurlin et al., 2005). In the Pamir, the Tanyamas suture is a south-verging thrust fault zone that has been inactive since the Cretaceous and there is no evidence for Eocene shortening north of the suture zone (Robinson, 2015), inconsistent with Eocene south-directed subduction.

We prefer the interpretation that the Eocene magmatic event is related to a series of drips (i.e., Rayleigh–Taylor instability) or delamination events in which Pamir–Tibetan mantle lithosphere and possibly lower crust was removed (e.g., Chen et al., 2013) (Fig. 8). The short-lived nature of the magmatic events and their ellipsoidal map-patterns are consistent with drip/delamination related magmatism (Ducea et al., 2013). MORB-normalized trace element patterns for Mesozoic and younger magmatic rocks show that the Central/South Pamir terrane lithosphere was modified by subduction processes (Fig. 3C). It is likely that the deep lithosphere was volatile-rich, particularly if the metasedimentary Karakul–Mazar terrane makes up a significant portion of the Central/South Pamir terrane lower crust. Depending on the rate of sinking, delaminated lithosphere may melt itself or may release fluids that produce melting in the overlying asthenosphere, mantle lithosphere, or crust (Elkins-Tanton, 2007; Ducea et al., 2013). Upwelling asthenosphere following the drip or delamination event may also result in adiabatic melting in the asthenosphere or dehydration melting in the lithosphere (Elkins-Tanton, 2007). The wide variety of plausible melt mechanisms associated with delamination is one of the challenges of recognizing delamination events or distinguishing these events from magmatism associated with intracontinental subduction, about which even less is known. High La/Yb and small or absent negative Eu anomalies in the Vanj magmatic complex (excepting one sample, 15–19, which has the geochemistry of a cumulate) and in the north Qiangtang magmatic complexes suggest melting in the absence of plagioclase and in the presence of amphibole and/or garnet, which occurs at high pressure ( $\geq 50$  km depth) (Ducea, 2002; Richards and Kerrich, 2007). Because the most mafic samples from the Vanj complex have the highest La/Yb, it is unlikely that fractional crystallization alone produced melts with adakitic compositions (Castillo et al., 2012). The high La/Yb Eocene melts could have originated from delaminated material, analogous to slab melts (Defant and Drummond, 1990), or from partial melting and differentiation in tectonically thickened crust. The moderately juvenile radiogenic isotopic composition of the Vanj complex rocks, the general lack of inherited zircon cores, the mantle-like zircon  $\delta^{18}\text{O}$ , and the  $\epsilon\text{Hf}$ – $\text{SiO}_2$  and Nd–Sr mixing models lead us to suggest that the Vanj complex melts originated in the asthenosphere and were emplaced into the lower Central/South Pamir terrane crust where the melts assimilated more evolved crustal material.

Recent numerical modeling studies of continental collisional orogens indicate that deformation in the mantle lithosphere tends

to accumulate adjacent to rheological boundaries, such as a between a relatively weak (low viscosity) accreted terrane and a relative strong (high viscosity) lithospheric block (Kelly et al., 2016; Z.H. Li et al., 2016). Subsequently the thickened mantle lithosphere may drip or delaminate along the rheological boundary because if its negative buoyancy (Kelly et al., 2016; Z.H. Li et al., 2016). Depending on the viscosity of the accreted terrane in the numerical model, density instabilities and mantle drips at the inboard edge of the accreted terrane begin to form 10–30 Myr after initial collision (Kelly et al., 2016; Z.H. Li et al., 2016), which is consistent with the time difference between initial India–Asia collision (~55 Ma) and the age of the Vanj complex (42–36 Ma). We propose that the Tanymas–Jinsha suture, which separates Mesozoic accreted terranes to the south from the para-autochthonous North Pamir/Kunlun terrane and Tarim block to the north, is a significant rheological boundary that focused mantle lithosphere thickening during India–Asia collision and led to a series of mantle drip or small delamination events in the Eocene.

#### 6.4. Miocene

The Pamir and Karakoram terranes experienced crustal anatexis, migmatization, and intrusion of leucogranite during the late Oligocene to Miocene. Zircon and titanite U–Pb crystallization ages for various leucogranite bodies in the Central Pamir gneiss domes range from 21–16 Ma and are as young as 7 Ma in the Shakh dara gneiss dome (Stearns et al., 2015; this study). Leucogranite in the Baltoro batholith, in the Karakoram metamorphic complex, has similar ages of 24–13 Ma (Searle et al., 2010). The evolved isotopic composition and the presence of inherited zircon cores in the Pamir leucogranite suggests partial melting of the lower Central/South Pamir terrane crust. Foundering or break-off of an Indian continental slab is postulated to have occurred at ~25 Ma beneath the Karakoram and heat from upwelling asthenosphere has been invoked to explain the origin of the Karakoram and Pamir leucogranite (Mahéo et al., 2009; Stearns et al., 2015). Leucogranite and migmatite are common in core complexes and gneiss domes globally in occurrences that are not necessarily associated with continental subduction or a slab-break off event (Whitney et al., 2013). Two alternative mechanisms to generate the Pamir leucogranite are: 1) dehydration melting from thermal relaxation and crustal heat production following crustal thickening (England and Thompson, 1984), and 2) near-isothermal decompression melting in response to crustal extension and rapid exhumation (Teyssier and Whitney, 2002). Peak metamorphic temperatures in the Central and South Pamir gneiss domes are  $\leq 800^\circ\text{C}$  (Stearns et al., 2015; Hacker et al., 2017) and the timing of leucogranite emplacement (24 to 7 Ma) slightly predate and overlap with exhumation ages (20 to 5 Ma) (Stübner et al., 2013; Rutte et al., 2017b), both of which support decompression melting during gneiss dome extension as a contributing mechanism.

#### 7. Conclusions

Studies of igneous rocks and detrital minerals from the Pamir Mountains record a rich history of magmatism during the Mesozoic and Cenozoic. New and compiled whole rock and detrital geochemical, isotopic, and geochronologic data help to identify and characterize the major magmatic events that have occurred in the Pamir during this time. These are presented below from oldest to youngest with estimates of their principal age ranges and zircon  $\varepsilon\text{Hf}_{(t)}$  equivalent isotopic values.

1) The Karakul–Mazar arc (250–200 Ma, with a peak in magmatism at 220–210 Ma;  $-2$  to  $-3$   $\varepsilon\text{Hf}_{(t)}$ ) is associated with

northward directed subduction of Paleotethys oceanic lithosphere beneath Asia.

- 2) The Rushan–Pshart arc (210?–170 Ma;  $-6$  to  $-7$   $\varepsilon\text{Hf}_{(t)}$ ) is associated with southward directed subduction of oceanic to transitional lithosphere of the Rushan–Pshart basin beneath the South Pamir terrane.
- 3) A prominent magmatic gap from 180 to 130 Ma reflects final accretion of the Karakoram, Central Pamir and South Pamir terranes and preceded the initiation of northward subduction of the Shyok basin.
- 4) The South Pamir batholith (120–100 Ma, with a high-flux event at ~105 Ma;  $-3$  to  $-15$   $\varepsilon\text{Hf}_{(t)}$ ) may be considered the northward extension of the Karakoram batholith, both of which are attributed to northward subduction of Shyok basin or Neotethyan oceanic lithosphere. Migration of magmatism into the South Pamir terrane is attributed to an episode of low-angle or flat slab subduction.
- 5) Relatively low-volume Late Cretaceous magmatism (80–70 Ma;  $-2$  to  $+2$   $\varepsilon\text{Hf}_{(t)}$ ) in the Pamir may record lithospheric extension in response to Neotethyan slab-roll back.
- 6) The Vanj magmatic complex (42–36 Ma;  $-4$  to  $+2$   $\varepsilon\text{Hf}_{(t)}$ ) is attributed to a mantle drip or delamination event induced by the collision between India and Asia.
- 7) Pamir gneiss dome (leucogranite) magmatism (20–10 Ma;  $-4$  to  $-8$   $\varepsilon\text{Hf}_{(t)}$ ) reflects crustal anatexis and is attributed at least in part to decompression melting during north-south directed extension and gneiss dome exhumation.
- 8) The Dunkeldik/Taxkorgan complex (12–10 Ma;  $-6$  to  $-10$   $\varepsilon\text{Hf}_{(t)}$ ) is associated with a localized mantle drip or delamination event.

Of these magmatic events, the Eocene Vanj complex and South Pamir batholith are particularly interesting because we interpret them to be along-strike equivalents of magmatic complexes in Tibet and thus manifestations of orogen-wide tectonic processes that operated for >2500 km along strike (Fig. 1). The tectonic processes are interpreted to be: 1) Early Cretaceous northward directed, low-angle to flat-slab subduction that includes a regional high-flux event during the Albian (110–105 Ma) and; 2) a series of mantle drips or localized delamination events during the Middle Eocene (~40 Ma) related to deformation and thickening of the mantle lithosphere along a rheological boundary represented by the Tanymas–Jinsha suture zone. Spatially restricted magmatism accompanying small mantle drip events may be characteristic of continental collisional orogens globally and the locus of drip or delamination magmatism in collisional orogens may be up to several hundred km away from the suture zone.

#### Acknowledgements

Funding was provided by: NSF EAR-1419748 (P.K.), NSF EAR-1450899 (B.C.), Romanian Executive Agency for Higher Education, Research, Development and Innovation Funding project PN-III-P4-ID-PCE-2016-0127 (M.N.D.), and an EarthScope Award for Geochronology Student Research (J.C.). Analytical support was provided by John Valley and Akizumi Ishida at WiscSIMS, George Gehrels and Mark Pecha at the Arizona Laserchron Center (supported by NSF EAR-1338583).

#### Appendix A. Supplementary material

Supplementary material related to this article can be found online at <https://doi.org/10.1016/j.epsl.2017.10.041>.

## References

- Allégre, C.J., Courtillot, V., Tapponnier, P., Hirn, A., Mattauer, M., Coulon, C., Jaeger, J.J., Achache, J., Schärer, U., Marcoux, J., Burg, J.P., Girardeau, J., Armijo, R., Gariépy, C., Gopel, C., Li, T.D., Xiao, X.C., Chang, C.F., Li, G.Q., Lin, B.Y., Teng, J.W., Wang, N.W., Chen, G.M., Han, T.L., Wang, X.B., Den, W.M., Sheng, H.B., Cao, Y.G., Zhou, J., Qiu, H.R., Bao, P.S., Wang, S.C., Wang, B.X., Zhou, Y.X., Ronghua, X., 1984. Structure and evolution of the Himalaya–Tibet orogenic belt. *Nature* 307, 17–22.
- Borneman, N.L., Hodges, K.V., Soest, M.C., Bohon, W., Wartho, J.A., Cronk, S.S., Ahmad, T., 2015. Age and structure of the Shyok suture in the Ladakh region of northwestern India: implications for slip on the Karakoram fault system. *Tectonics* 34, 2011–2033.
- Bouilhol, P., Jagoutz, O., Hanchar, J.M., Dudas, F.O., 2013. Dating the India–Eurasia collision through arc magmatic records. *Earth Planet. Sci. Lett.* 366, 163–175.
- Burg, J.P., 2011. The Asia–Kohistan–India collision: review and discussion. In: Brown, D., Ryan, P.D. (Eds.), *Arc–Continent Collision*. Springer, Berlin, Heidelberg, pp. 279–309.
- Burtman, V.S., Molnar, P., 1993. Geological and geophysical evidence for deep subduction of continental crust beneath the Pamir. *Spec. Pap., Geol. Soc. Am.* 281, 1–76.
- Carrapa, B., DeCelles, P.G., Wang, X., Clementz, M.T., Mancin, N., Stoica, M., Kraatz, B., Meng, J., Abdulov, S., Chen, F., 2015. Tectono-climatic implications of Eocene Paratethys regression in the Tajik basin of central Asia. *Earth Planet. Sci. Lett.* 424, 168–178.
- Carrapa, B., Mustapha, F.S., Cosca, M., Gehrels, G., Schoenbohm, L.M., Sobel, E.R., DeCelles, P.G., Russell, J., Goodman, P., 2014. Multisystem dating of modern river detritus from Tajikistan and China: implications for crustal evolution and exhumation of the Pamir. *Lithosphere* 6, 443–455.
- Castillo, P.R., 2012. Adakite petrogenesis. *Lithos* 134, 304–316.
- Chemenda, A.I., Burg, J.P., Mattauer, M., 2000. Evolutionary model of the Himalaya–Tibet system: geopoem: based on new modelling, geological and geophysical data. *Earth Planet. Sci. Lett.* 174, 397–409.
- Chen, J., Wu, J., Xu, J., Dong, Y., Wang, B., Kang, Z., 2013. Geochemistry of Eocene high-Mg# adakitic rocks in the northern Qiangtang terrane, central Tibet: implications for early uplift of the plateau. *Geol. Soc. Am. Bull.* 125, 1800–1819.
- Chen, S.S., Fan, W.M., Shi, R.D., Gong, X.H., Wu, K., 2017. Removal of deep lithosphere in ancient continental collisional orogens: a case study from central Tibet, China. *Geochim. Geophys. Geosyst.* 18, 1225–1243.
- Chen, Y., Zhu, D.C., Zhao, Z.D., Meng, F.Y., Wang, Q., Santosh, M., Wang, L.Q., Dong, G.C., Mo, X.X., 2014. Slab breakoff triggered ca. 113 Ma magmatism around Xainza area of the Lhasa Terrane, Tibet. *Gondwana Res.* 26, 449–463.
- Chung, S.L., Chu, M.F., Zhang, Y., Xie, Y., Lo, C.H., Lee, T.Y., Lan, C.Y., Li, X., Zhang, Q., Wang, Y., 2005. Tibetan tectonic evolution inferred from spatial and temporal variations in post-collisional magmatism. *Earth-Sci. Rev.* 68, 173–196.
- Corfield, R.I., Searle, M.P., Pedersen, R.B., 2001. Tectonic setting, origin, and obduction history of the Spontang Ophiolite, Ladakh Himalaya, NW India. *J. Geol.* 109, 715–736.
- Debon, F., Ali-Khan, N., 1996. Alkaline orogenic plutonism in the Karakorum batholith: the Upper Cretaceous KozSar complex (Karambar valley, N. Pakistan). *Geodin. Acta* 9, 145–160.
- Debon, F., Le Fort, P., Dautel, D., Sonet, J., Zimmermann, J.L., 1987. Granites of western Karakorum and northern Kohistan (Pakistan): a composite Mid-Cretaceous to upper Cenozoic magmatism. *Lithos* 20, 19–40.
- Defant, M.J., Drummond, M.S., 1990. Derivation of some modern arc magmas by melting of young subducted lithosphere. *Nature* 347 (6294), 662–665.
- Ding, L., Kapp, P., Zhong, D., Deng, W., 2003. Cenozoic volcanism in Tibet: evidence for a transition from oceanic to continental subduction. *J. Petrol.* 44, 1833–1865.
- Ducea, M.N., 2002. Constraints on the bulk composition and root foundering rates of continental arcs: a California arc perspective. *J. Geophys. Res., Solid Earth* 107 (B11).
- Ducea, M.N., Lutkov, V., Minaev, V.T., Hacker, B., Ratschbacher, L., Luffi, P., Schwab, M., Gehrels, G.E., McWilliams, M., Vervoort, J., Metcalf, J., 2003. Building the Pamirs: the view from the underside. *Geology* 31, 849–852.
- Ducea, M.N., Seclaman, A.C., Murray, K.E., Jianu, D., Schoenbohm, L.M., 2013. Mantle-drip magmatism beneath the Altiplano–Puna plateau, central Andes. *Geology* 41 (8), 915–918.
- Elkins-Tanton, L.T., 2007. Continental magmatism, volatile recycling, and a heterogeneous mantle caused by lithospheric gravitational instabilities. *J. Geophys. Res., Solid Earth* 112 (B3).
- England, P.C., Thompson, A.B., 1984. Pressure–temperature–time paths of regional metamorphism I. Heat transfer during the evolution of regions of thickened continental crust. *J. Petrol.* 25, 894–928.
- Fraser, J.E., Searle, M.P., Parrish, R.R., Noble, S.R., 2001. Chronology of deformation, metamorphism, and magmatism in the southern Karakoram Mountains. *Geol. Soc. Am. Bull.* 113, 1443–1455.
- Guo, Z., Wilson, M., Liu, J., Mao, Q., 2006. Post-collisional, potassic and ultrapotassic magmatism of the northern Tibetan Plateau: constraints on characteristics of the mantle source, geodynamic setting and uplift mechanisms. *J. Petrol.* 47, 1177–1220.
- Hacker, B., Luffi, P., Lutkov, V., Minaev, V., Ratschbacher, L., Plank, T., Ducea, M., Patiño-Douce, A., McWilliams, M., Metcalf, J.I.M., 2005. Near-ultrahigh pressure processing of continental crust: Miocene crustal xenoliths from the Pamir. *J. Petrol.* 46, 1661–1687.
- Hacker, B.R., Ratschbacher, L., Rutte, D., Stearns, M.A., Malz, N., Stübner, K., Kylander-Clark, A.R., Pfänder, J.A., Everson, A., 2017. Building the Pamir–Tibet Plateau—Crustal stacking, extensional collapse, and lateral extrusion in the Pamir: 3. Thermobarometry and petrochronology of deep Asian crust. *Tectonics* 36, 1743–1766.
- Hastie, A.R., Kerr, A.C., Pearce, J.A., Mitchell, S.F., 2007. Classification of altered volcanic island arc rocks using immobile trace elements: development of the Th–Co discrimination diagram. *J. Petrol.* 48, 2341–2357.
- Heuberger, S., Schaltegger, U., Burg, J.P., Villa, I.M., Frank, M., Dawood, H., Hussain, S., Zanchi, A., 2007. Age and isotopic constraints on magmatism along the Karakoram–Kohistan Suture Zone, NW Pakistan: evidence for subduction and continued convergence after India–Asia collision. *Swiss J. Geosci.* 100, 85–107.
- Hu, X., Garzanti, E., Wang, J., Huang, W., An, W., Webb, A., 2016. The timing of India–Asia collision onset – facts, theories, controversies. *Earth-Sci. Rev.* 160, 264–299.
- Jagoutz, O., Müntener, O., Ulmer, P., Pettker, T., Burg, J.P., Dawood, H., Hussain, S., 2007. Petrology and mineral chemistry of lower crustal intrusions: the Chilas Complex, Kohistan (NW Pakistan). *J. Petrol.* 48, 1895–1953.
- Ji, W.Q., Wu, F.Y., Chung, S.L., Wang, X.C., Li, Q.L., Liu, Z.C., Liu, X.C., Wang, J.G., 2016. Eocene Neo-Tethyan slab breakoff constrained by 45 Ma oceanic island basalt-type magmatism in southern Tibet. *Geology* 44, 283–286.
- Jiang, Y.H., Jiang, S.Y., Ling, H.F., Dai, B.Z., 2006. Low-degree melting of a metasomatized lithospheric mantle for the origin of Cenozoic Yulong monzogranite-porphphyry, east Tibet: geochemical and Sr–Nd–Pb–Hf isotopic constraints. *Earth Planet. Sci. Lett.* 241, 617–633.
- Jiang, Y.H., Liu, Z., Jia, R.Y., Liao, S.Y., Zhou, Q., Zhao, P., 2012. Miocene potassic granite–syenite association in western Tibetan Plateau: implications for shoshonitic and high Ba–Sr granite genesis. *Lithos* 134, 146–162.
- Jiang, Z.Q., Wang, Q., Wyman, D.A., Li, Z.X., Yang, J.H., Shi, X.B., Ma, L., Tang, G.J., Gou, G.N., Jia, X.H., Guo, H.F., 2014. Transition from oceanic to continental lithosphere subduction in southern Tibet: evidence from the Late Cretaceous–Early Oligocene (~91–30 Ma) intrusive rocks in the Chanang–Zedong area, southern Gangdese. *Lithos* 196, 213–231.
- Kapp, P., DeCelles, P.G., Gehrels, G.E., Heizler, M., Ding, L., 2007. Geological records of the Lhasa–Qiangtang and Indo-Asian collisions in the Nima area of central Tibet. *Geol. Soc. Am. Bull.* 119, 917–933.
- Kapp, P., Yin, A., Harrison, T.M., Ding, L., 2005. Cretaceous–Tertiary shortening, basin development, and volcanism in central Tibet. *Geol. Soc. Am. Bull.* 117, 865–878.
- Kelly, S., Butler, J.P., Beaumont, C., 2016. Continental collision with a sandwiched accreted terrane: insights into Himalayan–Tibetan lithospheric mantle tectonics? *Earth Planet. Sci. Lett.* 455, 176–195.
- Kemp, A.I.S., Hawkesworth, C.J., Collins, W.J., Gray, C.M., Blevin, P.L., 2009. Isotopic evidence for rapid continental growth in an extensional accretionary orogen: the Tasmanides, eastern Australia. *Earth Planet. Sci. Lett.* 284, 455–466.
- Khan, S.D., Stern, R.J., Manton, M.I., Copeland, P., Kimura, J.I., Khan, M.A., 2004. Age, geochemical and Sr–Nd–Pb isotopic constraints for mantle source characteristics and petrogenesis of Teru Volcanics, Northern Kohistan Terrane, Pakistan. *Tectonophysics* 393, 263–280.
- Lai, S.C., Qin, J.F., 2013. Adakitic rocks derived from the partial melting of subducted continental crust: evidence from the Eocene volcanic rocks in the northern Qiangtang block. *Gondwana Res.* 23, 812–824.
- Li, J., Niu, Y., Hu, Y., Chen, S., Zhang, Y., Duan, M., Sun, P., 2016. Origin of the late Early Cretaceous granodiorite and associated dioritic dikes in the Hongqilafu pluton, northwestern Tibetan Plateau: a case for crust–mantle interaction. *Lithos* 260, 300–314.
- Li, Z.H., Liu, M., Gerya, T., 2016. Lithosphere delamination in continental collisional orogens: a systematic numerical study. *J. Geophys. Res., Solid Earth* 121, 5186–5211.
- Liu, Z., Liao, S.Y., Wang, J.R., Ma, Z., Liu, Y.X., Wang, D.B., Tang, Y., Yang, J., 2017. Petrogenesis of late Eocene high Ba–Sr potassic rocks from western Yangtze Block, SE Tibet: a magmatic response to the Indo-Asian collision. *J. Asian Earth Sci.* 135, 95–109.
- Long, X., Wilde, S.A., Wang, Q., Yuan, C., Wang, X.C., Li, J., Jiang, Z., Dan, W., 2015. Partial melting of thickened continental crust in central Tibet: evidence from geochemistry and geochronology of Eocene adakitic rhyolites in the northern Qiangtang Terrane. *Earth Planet. Sci. Lett.* 414, 30–44.
- Mahéo, G., Blichert-Toft, J., Pin, C., Guillot, S., Pêcher, A., 2009. Partial melting of mantle and crustal sources beneath South Karakorum, Pakistan: implications for the Miocene geodynamic evolution of the India–Asia convergence zone. *J. Petrol.* 50, 427–449.
- McDonough, W.F., Sun, S.S., 1995. The composition of the Earth. *Chem. Geol.* 120, 223–253.
- Ou, Q., Wang, Q., Wyman, D.A., Zhang, H.X., Yang, J.H., Zeng, J.P., Hao, L.L., Chen, Y.W., Liang, H., Qi, Y., 2017. Eocene adakitic porphyries in the central-northern Qiangtang Block, central Tibet: partial melting of thickened lower crust and implications for initial surface uplifting of the plateau. *J. Geophys. Res., Solid Earth* 122, 1025–1053.

- Pearce, J.A., Parkinson, I.J., 1993. Trace element models for mantle melting: application to volcanic arc petrogenesis. *Geol. Soc. (Lond.) Spec. Publ.* 76, 373–403.
- Petterson, M.G., Treloar, P.J., 2004. Volcanostratigraphy of arc volcanic sequences in the Kohistan arc, North Pakistan: volcanism within island arc, back-arc basin, and intra-continental tectonic settings. *J. Volcanol. Geotherm. Res.* 130, 147–178.
- Replumaz, A., Negredo, A.M., Guillot, S., Villaseñor, A., 2010. Multiple episodes of continental subduction during India/Asia convergence: insight from seismic tomography and tectonic reconstruction. *Tectonophysics* 483, 125–134.
- Richards, J.P., Kerrich, R., 2007. Special paper: adakite-like rocks: their diverse origins and questionable role in metallogenesis. *Econ. Geol.* 102, 537–576.
- Robinson, A.C., 2015. Mesozoic tectonics of the Gondwanan terranes of the Pamir plateau. *J. Asian Earth Sci.* 102, 170–179.
- Robinson, A.C., Ducea, M., Lapen, T.J., 2012. Detrital zircon and isotopic constraints on the crustal architecture and tectonic evolution of the northeastern Pamir. *Tectonics* 31.
- Robinson, A.C., Yin, A., Manning, C.E., Harrison, T.M., Zhang, S.H., Wang, X.F., 2007. Cenozoic evolution of the eastern Pamir: implications for strain-accommodation mechanisms at the western end of the Himalayan–Tibetan orogen. *Geol. Soc. Am. Bull.* 119, 882–896.
- Roger, F., Tapponnier, P., Arnaud, N., Schaerer, U., Brunel, M., Zhiqin, X., Jingsui, Y., 2000. An Eocene magmatic belt across central Tibet: mantle subduction triggered by the Indian collision? *Terra Nova* 12, 102–108.
- Rutte, D., Lothar, R., Schneider, S., Stübner, K., Stearns, M.A., Gulzar, M.A., Hacker, B.R., 2017a. Building the Pamir–Tibetan Plateau—Crustal stacking, extensional collapse, and lateral extrusion in the Central Pamir: 1. Geometry and kinematics. *Tectonics* 36, 342–384.
- Rutte, D., Ratschbacher, L., Khan, J., Stübner, K., Hacker, B.R., Stearns, M.A., Enkelmann, E., Jonckheere, R., Pfänder, J.A., Sperner, B., Tichomirowa, M., 2017b. Building the Pamir–Tibetan Plateau—Crustal stacking, extensional collapse, and lateral extrusion in the Central Pamir: 2. Timing and rates. *Tectonics* 36, 385–419.
- Schwab, M., Ratschbacher, L., Siebel, W., McWilliams, M., Minaev, V., Lutkov, V., Chen, F., Stanek, K., Nelson, B., Frisch, W., Wooden, J.L., 2004. Assembly of the Pamirs: age and origin of magmatic belts from the southern Tien Shan to the southern Pamirs and their relation to Tibet. *Tectonics* 23.
- Searle, M.P., Parrish, R.R., Thow, A.V., Noble, S.R., Phillips, R.J., Waters, D.J., 2010. Anatomy, age and evolution of a collisional mountain belt: the Baltoro granite batholith and Karakoram Metamorphic Complex, Pakistani Karakoram. *J. Geol. Soc.* 167, 183–202.
- Searle, M.P., Windley, B.F., Coward, M.P., Cooper, D.J.W., Rex, A.J., Rex, D., Tingdong, L., Xuchang, X., Jan, M.Q., Thakur, V.C., Kumar, S., 1987. The closing of Tethys and the tectonics of the Himalaya. *Geol. Soc. Am. Bull.* 98, 678–701.
- Smit, M.A., Ratschbacher, L., Kooijman, E., Stearns, M.A., 2014. Early evolution of the Pamir deep crust from Lu–Hf and U–Pb geochronology and garnet thermometry. *Geology* 42, 1047–1050.
- Spurlin, M.S., Yin, A., Horton, B.K., Zhou, J., Wang, J., 2005. Structural evolution of the Yushu–Nangqian region and its relationship to syncollisional igneous activity, east-central Tibet. *Geol. Soc. Am. Bull.* 117, 1293–1317.
- Stearns, M.A., Hacker, B.R., Ratschbacher, L., Lee, J., Cottle, J.M., Kylander-Clark, A., 2013. Synchronous Oligocene–Miocene metamorphism of the Pamir and the north Himalaya driven by plate-scale dynamics. *Geology* 41, 1071–1074.
- Stearns, M.A., Hacker, B.R., Ratschbacher, L., Rutte, D., Kylander-Clark, A.R.C., 2015. Titanite petrochronology of the Pamir gneiss domes: implications for middle to deep crust exhumation and titanite closure to Pb and Zr diffusion. *Tectonics* 34, 784–802.
- Stübner, K., Ratschbacher, L., Weise, C., Chow, J., Hofmann, J., Khan, J., Rutte, D., Sperner, B., Pfänder, J.A., Hacker, B.R., Dunkl, I., 2013. The giant Shakhhdara migmatitic gneiss dome, Pamir, India–Asia collision zone: 2. Timing of dome formation. *Tectonics* 32, 1404–1431.
- Sui, Q.L., Wang, Q., Zhu, D.C., Zhao, Z.D., Chen, Y., Santosh, M., Hu, Z.C., Yuan, H.L., Mo, X.X., 2013. Compositional diversity of ca. 110 Ma magmatism in the northern Lhasa Terrane, Tibet: implications for the magmatic origin and crustal growth in a continent–continent collision zone. *Lithos* 168, 144–159.
- Sun, J., Xiao, W., Windley, B.F., Ji, W., Fu, B., Wang, J., Jin, C., 2016. Provenance change of sediment input in the northeastern foreland of Pamir related to collision of the Indian Plate with the Kohistan–Ladakh arc at around 47 Ma. *Tectonics* 35, 315–338.
- Sun, S.S., McDonough, W.S., 1989. Chemical and isotopic systematics of oceanic basalts: implications for mantle composition and processes. *Geol. Soc. (Lond.) Spec. Publ.* 42, 313–345.
- Teyssier, C., Whitney, D.L., 2002. Gneiss domes and orogeny. *Geology* 30, 1139–1142.
- Treloar, P.J., Rex, D.C., Guise, P.G., Coward, M.P., Searle, M.P., Windley, B.F., Petterson, M.G., Jan, M.Q., Luff, I.W., 1989. K–Ar and Ar–Ar geochronology of the Himalayan collision in NW Pakistan: constraints on the timing of suturing, deformation, metamorphism and uplift. *Tectonics* 8, 881–909.
- Vermeesch, P., 2012. On the visualisation of detrital age distributions. *Chem. Geol.* 312, 190–194.
- Vervoort, J.D., Patchett, P.J., Blichert-Toft, J., Albarède, F., 1999. Relationships between Lu–Hf and Sm–Nd isotopic systems in the global sedimentary system. *Earth Planet. Sci. Lett.* 168, 79–99.
- Vlasov, N., Yu, G., Dyakov, A., Cherev, E.S., 1991. Geological Map of the Tajik SSR and Adjacent Territories. Vsesojuznoi Geologic Institute of Leningrad, Saint Petersburg, Russia. Scale 1:500,000.
- Volkov, V.N., Shatagin, K.N., Kramchaninov, A.Y., 2016. On the role of contamination and hybridism in formation of the composite Raumid pluton granites (Pamir Mts.): results of Sm–Nd isotope study. *Dokl. Earth Sci.* 470, 981–984.
- Wang, Q., Wyman, D.A., Xu, J., Dong, Y., Vasconcelos, P.M., Pearson, N., Wan, Y., Dong, H., Li, C., Yu, Y., Zhu, T., 2008. Eocene melting of subducting continental crust and early uplifting of central Tibet: evidence from central-western Qiangtang high-K calc-alkaline andesites, dacites and rhyolites. *Earth Planet. Sci. Lett.* 272, 158–171.
- Whitney, D.L., Teyssier, C., Rey, P., Buck, W.R., 2013. Continental and oceanic core complexes. *Geol. Soc. Am. Bull.* 125, 273–298.
- Yin, A., Harrison, T.M., 2000. Geologic evolution of the Himalayan–Tibetan orogen. *Annu. Rev. Earth Planet. Sci.* 28, 211–280.
- Zanchi, A., Gaetani, M., 2011. The geology of the Karakoram range, Pakistan: the new 1:100,000 geological map of Central–Western Karakoram. *Ital. J. Geosci.* 130, 161–262.
- Zhu, D.C., Li, S.M., Cawood, P.A., Wang, Q., Zhao, Z.D., Liu, S.A., Wang, L.Q., 2016. Assembly of the Lhasa and Qiangtang terranes in central Tibet by divergent double subduction. *Lithos* 245, 7–17.
- Zhu, D.C., Mo, X.X., Niu, Y., Zhao, Z.D., Wang, L.Q., Liu, Y.S., Wu, F.Y., 2009. Geochemical investigation of Early Cretaceous igneous rocks along an east–west traverse throughout the central Lhasa Terrane, Tibet. *Chem. Geol.* 268, 298–312.
- Zhu, D.C., Wang, Q., Zhao, Z.D., Chung, S.L., Cawood, P.A., Niu, Y., Liu, S.A., Wu, F.Y., Mo, X.X., 2015. Magmatic record of India–Asia collision. *Sci. Rep.* 5, 14289.